3D imaging of subsurface magnetic permeability / susceptibility with portable frequency domain electromagnetic sensors for near surface exploration

Julien Guillemoteau, François-Xavier Simon, Guillaume Hulin, Bertrand Dousteyssier, Marion Dacko, Jens Tronicke

Geophysical Journal International

Geophys. J. Int. (2019) **219,** 1773–1785
Advance Access publication 2019 August 26
Marine geosciences and applied geophysics

doi: 10.1093/gji/ggz382

3-D imaging of subsurface magnetic permeability/susceptibility with portable frequency domain electromagnetic sensors for near surface exploration

Julien Guillemoteau [1], François-Xavier Simon [2], Guillaume Hulin,[3] Bertrand Dousteyssier,[4] Marion Dacko[4] and Jens Tronicke[1]

[1] *Universität Potsdam, Institut für Geowissenschaften, Karl-Liebknecht-Strasse* 24, 14476 *Potsdam-Golm, Germany. E-mail: julien@geo.uni-potsdam.de*
[2] *INRAP-Institut National de Recherches Archéologiques Préventives, UMR* 6249, *Chrono-Environnement Laboratory,* 9 *Rue Lavoisier,* 26000 *Besançon, France*
[3] *INRAP-Institut National de Recherches Archéologiques Préventives, Métis UMR* 7619, 121 *rue d'Alésia,* 75014 *Paris, France*
[4] *Université Clermont Auvergne, Maison des Sciences de l'Homme (USR* 3550*),* 4 *rue Ledru,* 63057 *Clermont-Ferrand, France*

Accepted 2019 August 22. Received 2019 August 20; in original form 2019 April 30

SUMMARY

The in-phase response collected by portable loop–loop electromagnetic induction (EMI) sensors operating at low and moderate induction numbers ($\leq$1) is typically used for sensing the magnetic permeability (or susceptibility) of the subsurface. This is due to the fact that the in-phase response contains a small induction fraction and a preponderant induced magnetization fraction. The magnetization fraction follows the magneto-static equations similarly to the magnetic method but with an active magnetic source. The use of an active source offers the possibility to collect data with several loop–loop configurations, which illuminate the subsurface with different sensitivity patterns. Such multiconfiguration soundings thereby allows the imaging of subsurface magnetic permeability/susceptibility variations through an inversion procedure. This method is not affected by the remnant magnetization and theoretically overcomes the classical depth ambiguity generally encountered with passive geomagnetic data. To invert multiconfiguration in-phase data sets, we propose a novel methodology based on a full-grid 3-D multichannel deconvolution (MCD) procedure. This method allows us to invert large data sets (e.g. consisting of more than a hundred thousand of data points) for a dense voxel-based 3-D model of magnetic susceptibility subject to smoothness constraints. In this study, we first present and discuss synthetic examples of our imaging procedure, which aim at simulating realistic conditions. Finally, we demonstrate the applicability of our method to field data collected across an archaeological site in Auvergne (France) to image the foundations of a Gallo-Roman villa built with basalt rock material. Our synthetic and field data examples demonstrate the potential of the proposed inversion procedure offering new and complementary ways to interpret data sets collected with modern EMI instruments.

Key words: Magnetic properties; Controlled source electromagnetics (CSEM); Electromagnetic theory; Environmental magnetism; Inverse theory.

1 INTRODUCTION

Portable frequency domain electromagnetic induction (EMI) loop–loop sensors are commonly used for sensing the electrical conductivity and the magnetic permeability (or susceptibility) of the subsurface. The loop–loop (also referred as Slingram) geometry consists of two coils, which act as a transmitting and a receiving magnetic dipole, respectively. The transmitter generates an oscillating primary electromagnetic field interacting with the subsurface and the receiver measures the resulting secondary magnetic field. By convention, the obtained datum is provided in the frequency domain as a complex ratio between the secondary magnetic field and the known primary magnetic field at the location of the receiver. Thus, the real part of this complex number reflects the in-phase *IP* response, while the imaginary part corresponds to the quadrature or out-of-phase *OP* response (both with regards to the phase of the primary excitation).

A basic procedure of interpretation is to analyse the electrical conductivity and the magnetic permeability of an effective homogeneous half-space from a single measurement (*IP*, *OP*), commonly

known as 'apparent' or 'half-space' conductivity/permeability. Several interpretation approaches including joint (Huang & Won 2000) and sequential (Guillemoteau *et al.* 2016) inversions of *IP* and *OP* data have been proposed to obtain such homogeneous half-space models for portable EMI sensor data. These methods use a full homogeneous half-space forward modeling procedure, that is, they robustly model the height and the geometry of the system for the full range of induction numbers. In this respect, they should be preferred to the approximate formula provided by McNeill (1980), which is valid only for very low induction numbers, zero elevation of the systems and horizontal/vertical coplanar loop geometries.

Modern multiconfiguration systems simultaneously record *IP* and *OP* data at different distances from the transmitter and/or for different orientations of the receiver. Thus, the resulting soundings contain information regarding different depths/volumes of investigation, and can therefore be inverted to reconstruct a heterogeneous model of subsurface electrical conductivity and magnetic permeability. Joint *IP–OP* layered inversion procedures were developed for airborne (Farquharson *et al.* 2003) and marine (Baasch *et al.* 2014) systems. Sasaki *et al.* (2010) also presented a joint 3-D *IP–OP* inversion procedure using synthetic data of a ground-based multifrequency EMI sensor. In addition, sequential inversion approaches have proved their applicability for loop–loop EMI sensor data because the effect of permeability and conductivity are rather well decoupled in the *IP–OP* data representation. The advantage of sequential approaches is the use of simple regularization settings in comparison to joint inversion approaches. In this respect, Guillemoteau *et al.* (2016) present a sequential *IP–OP* layered inversion strategy based on the following iterative procedure: (1) layered inversion of the OP data for the conductivity assuming a constant free air permeability model, (2) layered inversion of the IP data for the permeability using the conductivity model obtained at step 1, (3) layered inversion of the *OP* data with the model of permeability obtained at step 2, and so on, until a stable result is obtained. Later, Noh *et al.* (2018) proposed a similar sequential inversion procedure for the 3-D inversion of airborne EMI data.

Nevertheless, in most of practical cases, the single *OP* data is interpreted to only recover the subsurface electrical conductivity assuming that *OP* data are negligibly affected by the magnetic permeability. Ideally, the interpretation of *OP* data requires a 3-D non-linear forward modeling theory as done in Noh *et al.* (2014) for a focused target. However, because common portable EMI data sets contain several hundred thousand of data points, and cover an extended model space, the 3-D inversion using a full non-linear forward modeling theory is still a challenging task with standard computational resources. Linear and semi-linear approximations with a standard spatial domain formulation (Pérez-Flores *et al.* 2012; Kamm *et al.* 2013; Guillemoteau *et al.* 2015), which provides acceptable results for low to moderate induction numbers, were suggested to reduce the computation time. However, such approaches are also not applicable if setting a voxel-based 3-D model space that incorporate the resolution portable EMI sensor (10–20 cm) over hectare-scale areas.

For the case of portable EMI sensors, another issue is that most of today's field data sets are recorded with a too poor lateral overlap between individual soundings to envisage a multidimensional interpretation. The combination of this spatial undersampling and the opportunity to proceed to 1-D inversions approaches make this geophysical method largely underexploited in term of lateral resolution. In order to fulfil the basic sampling theorem for EMI data maps and with the aim to extract the finest lateral geological details from the data, Guillemoteau & Tronicke (2015) suggest to efficiently record densely sampled EMI data sets with a kinematic acquisition strategy, relying on continuous positioning at a cm-precision by an autotracking total station. This approach allows to properly sample 2-D and 3-D anomalies for each loop–loop configuration and, therefore, avoids typical difficulties encountered with undersampled data sets like a local 2-D or 3-D structure causing artefacts in a 1-D inversion result, which is non-detectable and non-removable if the spatial sampling is not sufficient. For interpreting EMI *OP* data collected at low to moderate induction numbers, Guillemoteau & Tronicke (2016) proposed a fast approximate 3-D forward modeling approach based on the Born approximation in the spectral-spatial domain to rapidly simulate large data sets consisting of more than 100 thousands soundings. This work led to a fast 3-D imaging method (Guillemoteau *et al.* 2017), which allows the near-instant 3-D voxel-based inversion of such *OP* data sets for a model consisting of around 100 million parameters.

In contrast with the conductivity problem, the magnetic susceptibility of the subsurface can be determined from the *IP* response with a linear theory (Noh *et al.* 2017; Thiesson *et al.* 2017; Klose *et al.* 2018). Indeed, the 'magnetization' fraction of the *IP* response, which is sensitive to the surrounding magnetic susceptibility, follows the magneto-static equations similarly to the magnetic method but with an active magnetic source. The use of a source actually offers the possibility to collect data with several configurations, which illuminate the subsurface with different sensitivity patterns and depth/volume extents. Thus, EMI *IP* data are not affected by the classical depth ambiguity, which is generally encountered for the passive geomagnetic method. Moreover, due to the use of a time-varying source, the *IP* response is not sensitive to the static remnant magnetization (Benech *et al.* 2002; Noh *et al.* 2017), which often represents a source of complexity for the inversion of passive geomagnetic data. In Noh *et al.* (2017), these points are discussed in more details using numerical experiments. They show that the inversion of *IP* data leads to more resolved and less ambiguous models of magnetic susceptibility than the inversion of passive geomagnetic data. In parallel, Klose *et al.* (2018) evaluated and demonstrated the applicability of a 3-D linear forward modeling approach and have applied it to explain field *IP* data collected with a portable multiconfiguration EMI sensor across a controlled permeable target. According to these different studies, multiconfiguration EMI *IP* measurements represent a promising method for imaging subsurface magnetic susceptibility variations.

Similarly to the case of the OP data, one needs very efficient inversion tools to interpret densely sampled *IP* data sets consisting of several hundred thousand of data points. A rapid 3-D linear inversion/deconvolution procedure was presented by Thiesson *et al.* (2017) for the case of a well- and even-determined inverse problem where the number of layers is limited by the number of non-redundant data at each sounding location. This parametric restriction is poorly adapted to the modeling of typical natural variations encountered over a large surveyed area. To overcome this problem, we propose to apply a 3-D full-grid multichannel deconvolution (MCD) procedure as introduced in Guillemoteau *et al.* (2017) for the case of *OP* data. This method can handle a 3-D voxel-based linear inversion subject to spatial smoothness constraints for a dense model grid and for large data sets as typically collected by portable EMI sensors. In the following, we first present the forward and the inverse modeling of *IP* data sets in the framework of a 3-D MCD procedure. Then, we present and discuss two synthetic examples of inversion, which aim at simulating realistic situations. Finally, we demonstrate the applicability of our method to field data collected

across an archaeological site in Auvergne (France) to image the remains of a Gallo-Roman villa.

2 THEORY

2.1 Theoretical in-phase data recorded by portable EMI sensors

We model the *IP* response of a loop–loop EMI sensor located above a conductive and permeable subsurface with (de Hoop 1995):

$$IP = IP^I + IP^M, \tag{1}$$

where IP^{I} is the induction fraction and IP^{M} is the magnetization fraction. For portable EMI sensors, which operate at low and moderate induction numbers (≤ 1), IP^{I} is relatively small so that the full *IP* data has been classically used for sensing the magnetic susceptibility of the subsurface (Tite & Mullins 1970; Tabbagh 1986; Simpson *et al.* 2010). Quantitative evaluations of the importance of the induction fraction in the *IP* responses can be found in Tabbagh (1985), Benech & Marmet (1999), and Noh *et al.* (2016). While IP^{I} is mostly influenced by the electrical conductivity of the subsurface and IP^{M} is mostly influenced by the magnetic susceptibility of the subsurface, these two parts are also subject to mutual coupling (Noh *et al.* 2016). Indeed, the magnetic susceptibility has a small influence on the dynamics of the eddy current, and the secondary magnetic field associated with the induction process interacts with the surrounding susceptibility. However, for typical near-surface applications, which involve the use of EMI sensors working at low to moderate induction numbers, and where the observed range of relative magnetic permeability μ_r is far below 1.1, these coupling effects can be neglected. In such conditions, Klose *et al.* (2018) have confirmed that the magnetization fraction shows a linear relation to subsurface magnetic susceptibility, and is negligibly affected by the electrical conductivity of the subsurface. According to these different aspects, we model the *IP* response collected by portable EMI sensors with

$$IP = IP^I + \iiint_{\mathrm{half-space}} \psi(x,y,z)\chi(x,y,z)\mathrm{d}x\mathrm{d}y\mathrm{d}z, \tag{2}$$

where we take the induction fraction IP^I for $\mu_r = 1$ (or a susceptibility $\chi = 0$) and ψ is the sensitivity function relating IP^M and the surrounding magnetic susceptibility, which is given by

$$\psi(x,y,z) = -\frac{\mathbf{H}_t.\mathbf{H}_r}{H_p}. \tag{3}$$

Here, $\mathbf{H}_t$ is the free-space magnetic field caused by the transmitter dipole, $\mathbf{H}_r$ is a fictitious free-space magnetic field caused by a dipole with the orientation and the position of the receiver, and H_p is the primary field used for computing the *IP* data. A detailed analysis of the different sensitivity functions of a portable four-configurations EMI sensor and a validation of such a linear forward modeling approach by comparison with a non-linear forward modeling approach are provided in Klose *et al.* (2018).

2.2 Extracting the information related to magnetization in practice

EMI data sets are nowadays routinely acquired with mobile setups to efficiently cover hectare scale areas, but also to minimize the variations in height and attitude of the sensor. Despite efforts to limit the noise inherent to the geometrical instability of the sensors, the *IP* responses remain affected by eventual constant shifts related to a miss-calibration of the sensor and time-dependent drifts, which are likely to be caused by a dilatation of the instrument shell in response to the ambient temperature (Delefortrie *et al.* 2014; Thiesson *et al.* 2014; Huang *et al.* 2017). That is, the *IP* response as collected by an EMI sensor may be more realistically described by

$$IP = IP^I + IP^M + C_1(t) + C_2, \tag{4}$$

where C_1 is the drift caused by the temporal change of ambient temperature and C_2 is the constant offset caused by an eventual miss-calibration of the instrument.

IP^I can be determined by taking the conductivity model derived from the inversion of the OP data. C_1 has long-term variations and can be easily detected and removed following the method described in Delefortrie *et al.* (2014). C_2 can be evaluated by using the method presented in Thiesson *et al.* (2014) or by calibrating the data with *in situ* magnetic susceptibility measurements (Delefortrie *et al.* 2018). An alternative approach to remove C_2 is to analyse map of the anomalous IP^{M} field similarly to Klose *et al.* (2018). Then, we can write

$$\Delta IP^M = \iiint_{\mathrm{half-space}} \psi(x,y,z)\Delta\chi(x,y,z)\mathrm{d}x\mathrm{d}y\mathrm{d}z, \tag{5}$$

where ΔIP^{M} is the difference with regards to the data at one reference point and $\Delta\chi$ is the model of magnetic susceptibility variation with regards to the model at the reference point. The reference point should ideally be taken in a homogeneous area with a susceptibility close to zero. One way to meet these conditions is to place the system as high as possible in air. If this is not feasible, a reference point may be found in the most homogeneous and less permeable part of the surveyed area, which is characterized by multiconfiguration IP^M curves presenting the smallest mean and variance. To do so, we select the sounding location that minimizes the following function Θ:

$$\Theta(x,y) = \sqrt{m^2(x,y) + \beta v(x,y)}, \tag{6}$$

where m and v are, respectively, the mean and the variance for the sounding curves in the vicinity of location (x,y), and β is a weighting factor.

2.3 Fast 3-D forward modeling of large data sets in the (k_x, k_y, z) domain

A typical EMI data set involves several hundreds of thousands data points collected across hectare-scale areas. In order to model such a large data set with an adequate resolution, we have to set up a large 3-D voxel-based model across the entire surveyed area. As an example, a model resolution of 10 cm across an area of one hectare and up to a depth of 5 m requires 50 millions parameters.

As presented above, the sensitivity function does not depend on the subsurface distribution of permeability (i.e. the problem is linear), and, moreover, the data can be acquired with a sensor at a fixed height. Thanks to these two aspects, we can consider the sensitivity function as constant across the entire surveyed area and write the problem as a 2-D horizontal convolution between the sensitivity function and the 3-D subsurface model of magnetic susceptibility. Accordingly, we model measurements collected at the positions (x', y') above a 3-D subsurface model of magnetic susceptibility $\chi(x,y,z)$ with

$$IP^M(x',y') = \iiint_{half space} \psi(x'-x, y'-y, z)\chi(x,y,z)dxdydz. \tag{7}$$

By considering a discrete vertical distribution made of N_z layers for the susceptibility model, we have

$$IP^M(x', y') = \sum_{l=1}^{N_z} \iint_{halfspace} \psi^l(x' - x, y' - y)\chi^l(x, y)dxdy, \quad (8)$$

where ψ^l is the 2-D sensitivity function of the lth layer with the interfaces at depths z_l and z_{l+1} given by

$$\psi^l(x, y) = \int_{z_l}^{z_{l+1}} \psi(x, y, z)\mathrm{d}z. \quad (9)$$

By performing a double Fourier transform of this expression, we obtain

$$\tilde{IP}^M(k_x, k_y) = \sum_{l=1}^{N_z} \tilde{\psi}^l(k_x, k_y)\tilde{\chi}^l(k_x, k_y). \quad (10)$$

where $\tilde{}$ denotes the 2-D Fourier transform ($x \rightarrow k_x, y \rightarrow k_y$). Thus, by considering a discrete $N_x \times N_y$ model distribution in the lateral directions, $\tilde{\psi}^l$ and $\tilde{\chi}^l$ can be computed with a 2-D discrete Fourier transform of the function ψ^l and χ^l, respectively. To efficiently model a large amount of data and for a fine 3-D model grid, a single 2-D inverse Fourier transform of eq. (10) is required. Such an approach is much faster than computing the integral in the spatial domain (as in eq. 7) for every data points of a map.

2.4 Fast 3-D inverse modeling of large data sets in the (k_x, k_y, z) domain

We consider the problem of jointly inverting N_c maps of IP^M data, where N_c is the number of different configurations; that is, different transmitter-receiver geometries like horizontal/vertical coplanar (HCP/VCP) or perpendicular configurations with a receiver oriented in the in-line direction (PERP), and variations in further acquisition parameters such as variations in loop separation s, system height h, or even the pitch, the roll, and the yaw (Guillemoteau & Tronicke 2015) of the system. To invert such large multiconfiguration data sets for a 3-D distribution of magnetic susceptibility $\chi(x, y, z)$, we use the 3-D multichannel deconvolution (MCD) method with smoothness constraints (Guillemoteau *et al.* 2017).

The principle of the MCD approaches is to benefit from the horizontal convolution feature of the forward problem to speed up the solving of the inverse problem (Li & Oldenburg 1992; Møller *et al.* 2001). This is done by formulating a voxel-based 3-D linear inversion problem with spatial smoothness constraints in the hybrid spectral-spatial domain (k_x, k_y, z) as described in the following global cost function Φ_g (Guillemoteau *et al.* 2017)

$$\Phi_g = \int_{-\infty}^{\infty}\int_{-\infty}^{\infty} |\tilde{\Phi}_d|^2 + |\tilde{\Phi}_m^x|^2 + |\tilde{\Phi}_m^y|^2 + |\tilde{\Phi}_m^z|^2 \mathrm{d}k_x\mathrm{d}k_y. \quad (11)$$

Here, the first term inside the integral is the data misfit term, which is given by

$$|\tilde{\Phi}_d(k_x, k_y)|^2 = \sum_{i=1}^{N_c} \left[\tilde{IP}_i^{M,Obs}(k_x, k_y) - \tilde{IP}_i^{M,Mod}(k_x, k_y)\right]^2, \quad (12)$$

where $\tilde{IP}_i^{M,Mod}$ is calculated by eq. (10). The other terms inside the integral (eq. 11) represent the spatial smoothness constraints given by

$$|\tilde{\Phi}_m^x(k_x, k_y)|^2 = \lambda_x \int_0^{\infty} \left[\tilde{s}(k_x)\tilde{\chi}(k_x, k_y, z)\right]^2 \mathrm{d}z, \quad (13)$$

$$|\tilde{\Phi}_m^y(k_x, k_y)|^2 = \lambda_y \int_0^{\infty} \left[\tilde{s}(k_y)\tilde{\chi}(k_x, k_y, z)\right]^2 \mathrm{d}z, \quad (14)$$

and

$$|\tilde{\Phi}_m^z(k_x, k_y)|^2 = \lambda_z \int_0^{\infty} \left[\tilde{\chi}(k_x, k_y, z) - \tilde{\chi}(k_x, k_y, z + \Delta z)\right]^2 \mathrm{d}z. \quad (15)$$

Here, λ_x, λ_y and λ_z are the damping factors characterizing the relative importance of the spatial smoothness constraints with respect to the data misfit term and s is a difference of Dirac-delta function. For example, if we consider the x direction, we have

$$s(x) = \delta(x + \Delta x) - \delta(x). \quad (16)$$

When considering a discrete model-grid composed of $N_x \times N_y \times N_z$ voxels, Guillemoteau *et al.* (2017) provide the solution $\tilde{\chi}(k_x, k_y, z)$, which simultaneously minimizes $\tilde{\Phi}_d$ and $\tilde{\Phi}_m^{x,y,z}$ for every spectral point (k_x, k_y):

$$\tilde{\chi}(k_x, k_y, [z_1 \cdots z_l \cdots z_{N_z}]) = \left(\tilde{\mathbf{G}}^T\tilde{\mathbf{G}} + \mathbf{S}\right)^{-1} \tilde{\mathbf{G}}^T\tilde{\mathbf{IP}}^{\mathbf{M,Obs}}, \quad (17)$$

where $\tilde{\mathbf{G}}$ is a $N_c \times N_z$ matrix containing $\tilde{\psi}_i^l(k_x, k_y)$, and $\mathbf{S}$ is a $N_z \times N_z$ smoothness matrix given by

$$\mathbf{S} = \lambda_x^2|\tilde{s}_1(k_x)|^2\mathbf{D}^T\mathbf{D} + \lambda_y^2|\tilde{s}_1(k_y)|^2\mathbf{D}^T\mathbf{D} + \lambda_z^2\mathbf{D}^T\mathbf{D}\mathbf{L}^T\mathbf{L}. \quad (18)$$

Here, $\mathbf{D}$ is a diagonal matrix containing the layer thicknesses of the 3-D model grid, and $\mathbf{L}$ is the first order 1-D smoothness matrix applied to the vertical direction of the model. After this problem is solved for every spectral number (k_x, k_y), Φ_g is by fact also minimized as it is a sum over k_x and k_y of the functions $\tilde{\Phi}_d$ and $\tilde{\Phi}_m^{x,y,z}$. The resulting 3-D distribution of the magnetic susceptibility in the spatial domain is obtained by performing a double inverse Fourier transform $\mathcal{F}^{-1}$ of the ensemble of solutions in the (k_x, k_y) domain

$$\chi(x, y, [z_1 \cdots z_l \cdots z_{N_z}]) = \mathcal{F}^{-1}\left[\tilde{\chi}(k_x, k_y, [z_1 \cdots z_l \cdots z_{N_z}])\right]. \quad (19)$$

The inversion of ΔIP^M data follows the same procedure. First, the data are inverted for each (k_x, k_y) point

$$\tilde{\Delta\chi}(k_x, k_y, [z_1 \cdots z_l \cdots z_{N_z}]) = \left(\tilde{\mathbf{G}}^T\tilde{\mathbf{G}} + \mathbf{S}\right)^{-1} \tilde{\mathbf{G}}^T\tilde{\Delta\mathbf{IP}}^{\mathbf{M,Obs}}. \quad (20)$$

Then, the result is given in the spatial domain by

$$\Delta\chi(x, y, [z_1 \cdots z_l \cdots z_{N_z}]) = \mathcal{F}^{-1}\left[\tilde{\Delta\chi}(k_x, k_y, [z_1 \cdots z_l \cdots z_{N_z}])\right]. \quad (21)$$

The 3-D MCD approach consists of performing $N_x \times N_y$ inversions with kernels of size $N_c \times N_z$. This method requires much less memory and is much faster than a 3-D inversion in the spatial domain, which considers $N_c \times N_x \times N_y$ data and $N_x \times N_y \times N_z$ parameters, and would require the inversion of a $(N_c \times N_x \times N_y) \times (N_x \times N_y \times N_z)$ matrix. In practice, the 3-D MCD method allows the near-instant voxel-based inversion of large data sets. Moreover, it allows the use of a fine and extended 3-D grid to optimally describe the distribution of magnetic susceptibility $\chi(x, y, z)$ within the subsurface. It is important to mention that the 3-D MCD approach requires that the data maps follow the same horizontal grid as used for the subsurface model of magnetic susceptibility. This means that the observed maps have to be interpolated according to the chosen model grid. In fact, to avoid interpolation artefacts, the

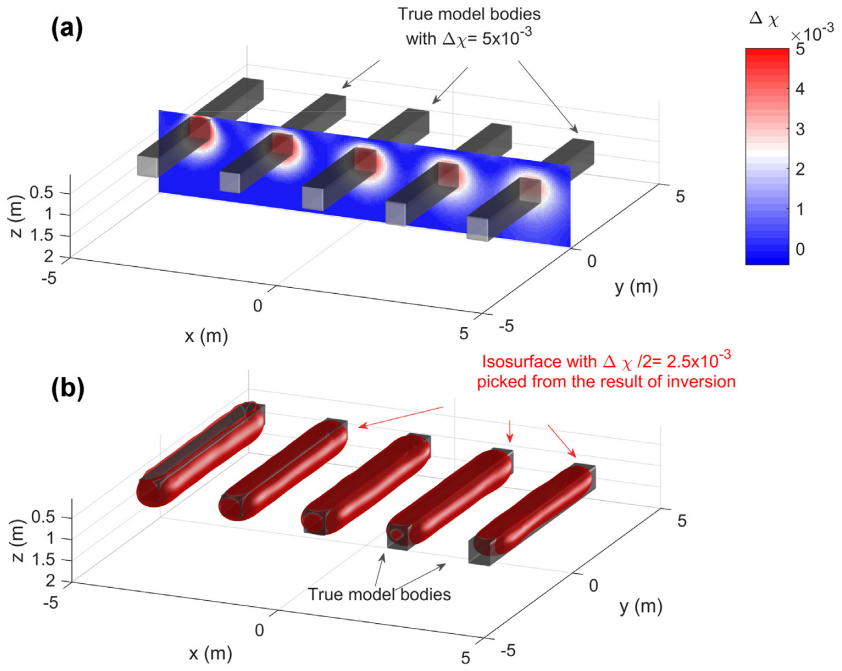

Figure 1. First synthetic experiment: comparison between the model of magnetic susceptibility provided by the 3-D MCD method and the true model of susceptibility, which was used to generate the synthetic data. The true model of magnetic susceptibility consists of 5 rectangular bodies of size 0.5 m × 5 m × 0.5 m whose tops are located at different depths (0.1, 0.25, 0.4, 0.55 and 0.7 m) and showing a contrast of $\Delta\chi = 0.005$ with regard to the homogeneous background. (a) Vertical slice at $y = 0$ m compared with the true rectangular structures (in purple-red). (b) Isosurface plot $\Delta\chi/2$ (in red) compared with the true rectangular structures (in grey).

data maps must fulfill the sampling theorem in the horizontal direction, while the model grid must be fine enough in the horizontal direction to capture all the information contained in these maps. This mutual condition between the data set and the model grid is inherently imposed by the 3-D MCD approach. In fact, these conditions, which result from the Fourier transformation of both data and model space, allow to prevent any kind of aliasing effect from the imaging procedure. Accordingly, it should be pointed out that the fulfillment of these conditions should always be looked for to optimally set up a voxel-based inversion procedure even with a standard spatial domain formulation, where a coarse lateral sampling may results in a poor lateral overlap of the shallowest measurements, and therefore in high imaging ambiguities close to the surface.

3 SYNTHETIC EXPERIMENTS

We generate synthetic ΔIP maps by performing a double inverse Fourier transform of eq. (10) for a model of anomalous magnetic susceptibility $\Delta\chi$. We consider a four-receivers loop–loop EMI system located at a height of 0.2 m above ground and operating with a single 9 kHz horizontal source-coil. Two horizontal receiver-coils are located at 1 m and 2 m inline distance from the source, representing the horizontal coplanar geometries HCP1 and HCP2. Furthermore, two vertical receiver-coils, for which the magnetic dipole points towards the inline direction, are located at 1.1 and 2.1 m inline distance from the source, representing the perpendicular geometries PERP1.1 and PERP2.1.

The chosen model is a 12 m × 12 m × 15 m rectangular grid of magnetic susceptibility contrasts $\Delta\chi$. The voxels composing the grid have a size of 0.025 m × 0.025 m × d_z where d_z is the layer thickness, which is set to 0.01 m from 0 to 0.4 m depth, 0.02 m from 0.4 to 2 m, and then d_z linearly increases until the maximum depth of 15 m. We use this rather fine grid to ensure that the highest frequencies of the ψ function are properly modeled through the presented spectral domain modeling. This setting yields four maps with a fairly dense sampling (0.025 m × 0.025 m) if compared to a realistic acquisition sampling. In order to simulate more realistic conditions, we take a subsample of the resulting map with in- and crossline sounding point spacing of 0.1 and 0.5 m, respectively. In the same goal, we finally apply a 50 ppm uncorrelated random noise to each datum. In practice, the functions ψ are computed one time for one EMI system at a given height and a given orientation, and stored. When having the pre-computed functions ψ, the generation of the four maps takes around half a minute with 16 GB RAM and a 2.80 GHz CPU.

We perform a first synthetic experiment with a model of magnetic susceptibility consisting of five rectangular bodies whose tops are located at 0.1, 0.25, 0.4, 0.55 and 0,7 m. These rectangular structures have a cross-sectional surface of 0.5 m × 0.5 m, a length of 5 m, and show a contrast of $\Delta\chi = 0.005$ with respect to the homogeneous background. For the 3-D MCD of the resulting synthetic data, we consider a grid of 20 m × 20 m × 2 m with cubic voxels of size 0.05 m × 0.05 m × 0.05 m. As discussed above, the 3-D MCD method requires that the data maps follow the same horizontal sampling as the model grid. Thus, and to actually simulate the procedure for real field data, we re-sample the noisy synthetic data (of resolution 0.1 m x 0.5 m) to a grid with a resolution of 0.05 m× 0.05 m by a linear interpolation. The resulting maps are then inverted using the 3-D MCD procedure. The inversion takes 140 seconds on a 2.80 GHz CPU with 16 GB RAM. The resulting voxel-based model of magnetic susceptibility is shown together with the true model in Fig. 1. The shape and the depth of the rectangular structures are well reconstructed by the smooth model obtained with the 3-D MCD method although the width of the rectangular structures and

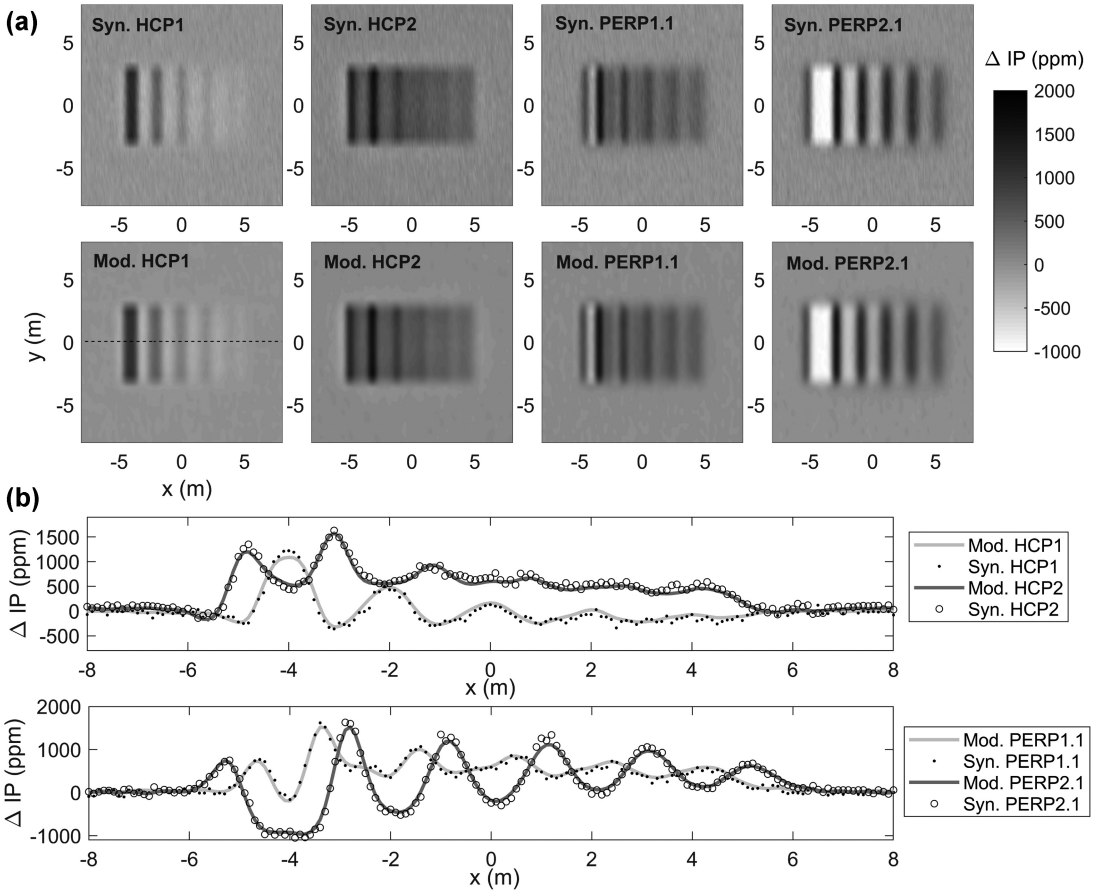

Figure 2. First synthetic experiment: comparison between the noisy input synthetic data and the modeled data computed after inversion. (a) The four maps of input (top) and modeled (bottom) data, the mean RMS error is 53 ppm and is consistently comparable to the random noise of 50 ppm, which was added to each synthetic datum. (b) Example of the profile $y = 0$ m passing above the centre of the rectangular bodies. Top: HCP1 and HCP2 configurations, bottom: PERP1.1 and PERP2.1 configurations.

the distances between them, are smaller than the lateral footprint of the soundings. As illustrated in Fig. 2a, this synthetic model results in a rather complex multiconfiguration EMI response, which is hardly understandable by a visual inspection of the data. It is also obvious that a 1-D layered inversion of such data would lead to severe imaging artifacts, which are likely to make the interpretation even more difficult than the non-inverted maps. The 3-D MCD approach permits the correct interpretation of such high-resolution EMI signal and therefore leads to a significant improvement in term of imaging capabilities. Importantly, this result is obtained with a statistically pertinent data misfit of mean RMS error of 53 ppm (see Fig. 2), which was obtained by following a basic Occam's principle (Constable *et al.* 1987). This means that no sophisticated prior information is required, making the overall imaging procedure rather simple and versatile.

We perform a second synthetic experiment by following the same procedure as for the previous experiment (i.e. we subsample the synthetic data in the same way and add the same uncorrelated noise), but for a different input susceptibility model (Figs 3 and 4). For this second test, we simulate a low susceptibility deposit covering a more permeable bedrock as it may be found in a volcanic environment. We set a contrast of $\Delta\chi = 0.01$ between the bedrock formation and the overburden. The depth of the overburden-bedrock interface varies between 0 and 2 m, and laterally at different spatial scales as shown in Fig. 3a and 3b. For the considered four-configuration EMI sensor, the resulting in-phase maps are shown in Fig. 4a. The four graphics illustrate how different configurations respond to the heterogeneous input model. Note that the HCP1 data show a reverse sign compared to the other three channels, except at locations where the interface is close to the surface. This is explained by a negative vertical sensitivity for this configuration at depths larger than 40 cm (Klose *et al.* 2018). This example illustrates that the interpretation of a single data map (e.g. recorded using the popular HCP1 configuration) can be limited in view of the true distribution of magnetic susceptibility within the subsurface.

In an attempt to overcome this difficulty, we apply the same procedure as for the first experiment (i.e. the MCD algorithm with the same inversion setting) to invert this four-configuration synthetic data set. The data misfit, which is shown in Fig. 4, follows the same characteristics as for the previous synthetic case. When dealing with a smooth inversion model, one basic guess is to associate the true position of interfaces where anomalies show half of their true values. As such, we extract an isosurface with the value $\Delta\chi/2 = 0.005$ from the resulting 3-D voxel-based model (shown in Fig. 3c) and compare it with the true interface in Fig. 3b. As expected, the MCD method could reproduce well the true interface up to submetre wavelengths. Similarly to the first synthetic experiment, the second experiment shows that our method is able to image lateral variations of the magnetic susceptibility at a scale that is much smaller than the lateral footprint of the soundings (which is around 4–6 m for an

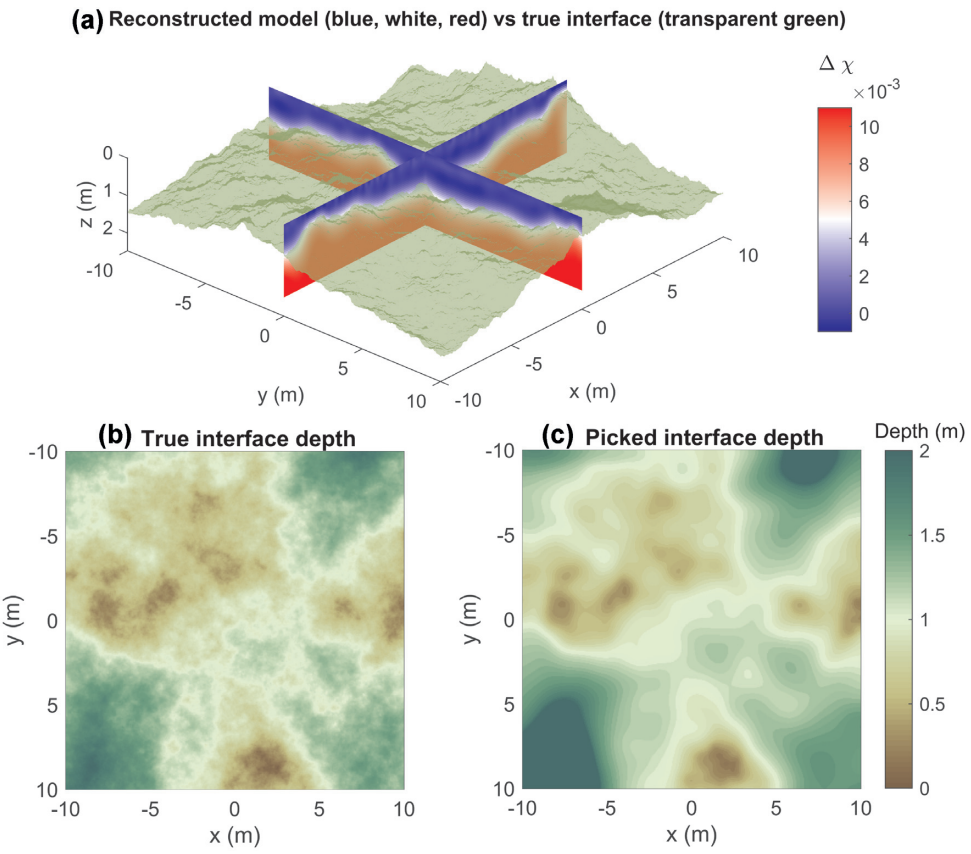

Figure 3. Second synthetic experiment: comparison between the true model of susceptibility, which was used to generate the synthetic data, and the model of magnetic susceptibility provided by the 3-D MCD method. The true model consists of two layers, which aim at simulating a rather poorly permeable soil cover deposited over a more permeable bedrock (e.g. as in a volcanic region). The second layer makes a contrast $\Delta\chi = 0.01$ with regard to the first layer. (a) 3-D subsurface model of magnetic susceptibility contrast obtained with 3-D MCD method compared with the interface (in transparent green) of the true input model. (b) Depth of the interface between the two layers. (c) Reconstructed depth of the interface corresponding to the isosurface picked at $\Delta\chi/2 = 0.005$ in the smooth model, which was provided by the 3-D MCD method.

inter-coil distance of 2 m). This second synthetic experiment shows particularly that our 3-D voxel-based imaging procedure is able to image a complex subsurface magnetic susceptibility distribution, which could not be handled with a one dimensional interpretation or a 3-D parametric inversion (e.g. using simple-shape 3-D anomalous bodies).

These two synthetic examples show that our inversion approach significantly improves the imaging capabilities compared to standard 1-D approaches, which are, by definition, limited to the lateral footprint of the sounding (i.e. approximately 2–2.5 times the largest intercoil distance). Thanks to the voxel-based parametrization of the inverse problem, our method can handle complex and rather smale-scale spatial variations of magnetic susceptibility. Moreover, because the regularization strategy follows the basic Occam's concept, the same simple inversion setting can be adopted to different subsurface environments. This makes our method a simple and versatile tool to image the magnetic susceptibility of the subsurface with a rather high resolution and with an efficient computing time.

4 FIELD EXPERIMENT

4.1 Field site

We apply our 3-D MCD method to field data collected with a multi-configuration EMI sensor at the archaeological site of Lieu Dieu, in La Sauvetat, Massif Central (France). The site is located on a flood plain area east of the lava dome chain 'Chaîne des Puys' (Figs 5a and b). The plain area is punctuated by low hills, which are made of layered carbonate sediments, and covered by basalt lava flows. The Lieu Dieu's site is located near the *Plateau de Gergovie* and the *Plateau de Corent* hills. During the second half of the 19th century, the Lieu Dieu locality has provided architectural and decorative elements of Roman styling. Between 1968 and 1998, several pedestrian archaeological surveys suggested the presence of an antic rural domain (Vallat 2002). Between 2004 and 2015, seven aerial surveys provided a first partial plan of the domain, and were complemented in 2015 by an extensive single-configuration electromagnetic survey (with a GSSI EMP400 profiler) over more than 5 hectares (Simon *et al.* 2016). The resulting apparent magnetic susceptibility map together with the aerial photographies unveiled one of the most extended rural villa of the Arverni's territory. This villa was occupied without discontinuity during the first five centuries of our era, which correspond to the Gallo-Roman period in this area. In this study, we focus on the residential part of the villa, which was kept for the rich family of the owner. This part is composed of multiple rooms structured around an internal courtyard. The buried foundations are mainly built with nearby basalt rocks, which produce temporal changes of colour vegetation (Figs 5c and d), and which respond well to EMI in-phase soundings due to their high magnetic susceptibility as previously evaluated by Simon *et al.* (2016).

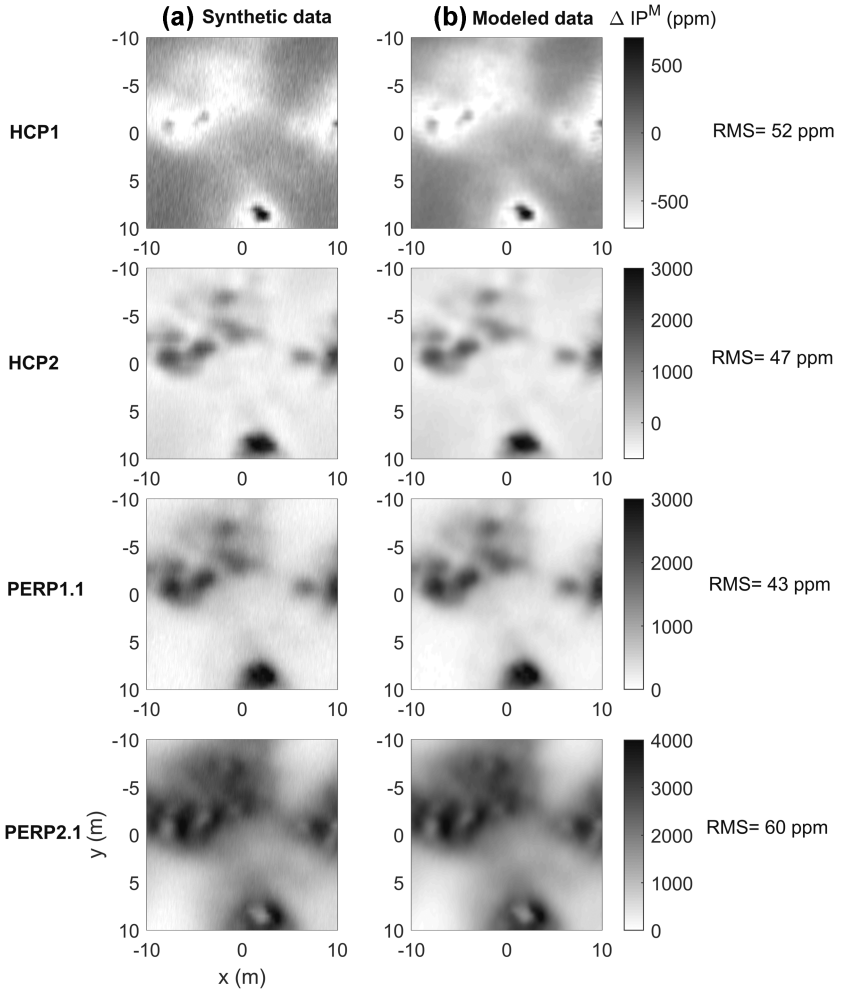

Figure 4. Second synthetic experiment: comparison between (a) the input synthetic data contaminated with a random noise of 50 ppm and (b) the modeled data computed after the 3-D MCD inversion. On the right side, we show the mean RMS error for each channel map.

4.2 Data acquisition

We collected our multiconfiguration EMI in-phase data set with a DUALEM21s system. This portable EMI sensor has the same characteristics as the four-configuration sensor used in the synthetic experiments. We collected the data at a height $h = 0.2$ m above ground, which is similar to the height considered for the synthetic experiments. To reduce noise caused by variations in height and in sensor orientation, we mount the DUALEM21s system on a non-conductive and non-magnetic cart. The cart is automatically located with a centimetric precision by an autotracking total station following the procedure described in Böniger & Tronicke (2010). This allows for the optimal lateral resolution as required for gridding the data. To record our data set, we acquire a set of adjacent parallel profiles separated by a distance of 0.5 m. By continuously collecting the data at a rate of 5 Hz at walking speed, we obtain an average distance of 0.1 m between individual soundings in the in-line direction.

It is important to note that the in-line shape of the PERP response depends on the heading of the sensor. This is due to the fact that the PERP configurations show sensitivity patterns that are non-symetric in the in-line direction (Guillemoteau *et al.* 2017; Klose *et al.* 2018). To first improve the consistency between adjacent profiles and hence to have more readable maps, and because our 3-D MCD method can only be applied to unidirectional profiles, we record the data with a sensor that is always pointing towards the same x-direction. In practice, this demands us to alternate pushing and pulling the cart from one profile to the adjacent one.

4.3 Data pre-processing

We apply several pre-processing steps to make the field data sets ready for an inversion with our 3-D MCD method. No temporal drift $C_1(t)$ was observed in the portion of data analysed in this study. In order to remove the induction fraction of the in-phase response, we first invert the out-of-phase data to recover the 'half-space' or 'apparent' electrical conductivity of the subsurface (Guillemoteau *et al.* 2016). Then, we use the result of this half-space inversion to estimate the in-phase induction fraction IP^I and to remove it from the total in-phase response. Since the remaining IP^M response is potentially affected by a constant shift C_2, we consider an anomalous ΔIP^M field with respect to a reference point, which is selected in the most homogeneous and least permeable area. Finally, the ΔIP^M field is gridded to fulfil the sampling condition imposed by the 3-D MCD method. These different steps are illustrated in Fig. 6 for the case

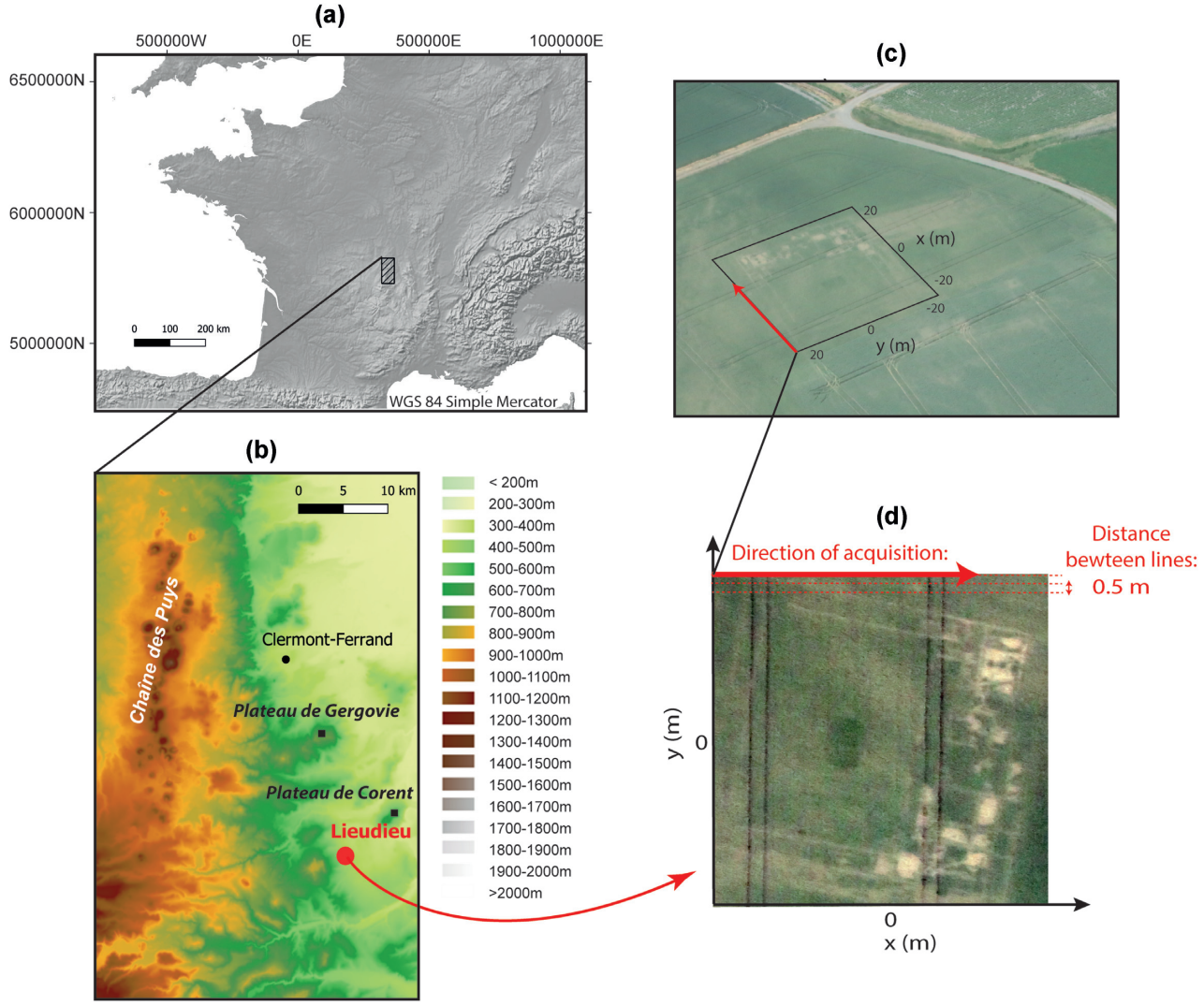

Figure 5. Field experiment at Lieu Dieu's archaeological site. (a) Localization of the volcanic chain 'Chaine des Puys' in Western Europe. (b) Localisation of the Lieu Dieu's field site in a local topographic map (source: http://wms.craig.fr). (c) Aerial photography unveiling the buried foundations of a Gallo-Roman villa through a transitory (seasonal) change in colour vegetation. In black, we show the fraction of the Gallo-Roman villa covered by the EMI data with the local coordinate system of the geophysical survey. (d) Aerial photography cropped on the surveyed area and rotated in order to schematically show how the surveyed fraction of the Gallo-Roman villa is positioned in the local coordinate system of the geophysical survey.

of the HCP2 channel, which shows the largest induction fraction as expected from its induction number (see Klose *et al.* 2018).

4.4 Qualitative interpretation of the data

In Fig. 7a, we show pre-processed data. The four data maps unveil a complex system of individual rooms for the Eastern part, and a well-delimited large courtyard in the centre and Western part. The channels are displayed from top to bottom following an increasing depth of investigation, according to the vertical sensitivity analysis in Klose *et al.* (2018).

The shallowest HCP1 channel has the particularity to show negative anomalies above the walls, while the other channels show positive responses. As discussed in the second synthetic case, because the HCP1 channel shows a positive sensitivity pattern only for depth <40 cm, this result indicates that the walls are not likely to be shallower than 30–40 cm. Analysing the data recorded with the PERP1.1 configuration, which is able to detect deeper structures and which has a significant positive sensitivity pattern at depths larger than 10 cm (Klose *et al.* 2018), leads to the same conclusion. Similarly, the fact that the HCP2 channel shows rather simple mono-sign responses actually indicates that the walls may not be found directly close to the ground surface but at a depth where its sensitivity pattern show a mono-sign distribution in the lateral direction, that is, at depths larger than 20 cm according to Klose *et al.* (2018). For the PERP2.1 channel, which has the deepest sensitivity (sensing up to a depth of 2.5 m), the responses above the walls are more complex as expected from the rather complex lateral distribution of its sensitivity at a depth smaller than 1 m.

We also observe that the two PERP1.1 and PERP2.1 channels, which sense the subsurface susceptibility at the deepest levels, show a negative anomaly near the centre of the courtyard (at the position $x = -5$ m, $y = 0$ m). Theoretically, this could be caused by either a permeable body near the surface (because the PERP1.1 and PERP2.1 have negative sensitivities near the surface between the coils) or a less permeable body at a larger depth. Thanks to the

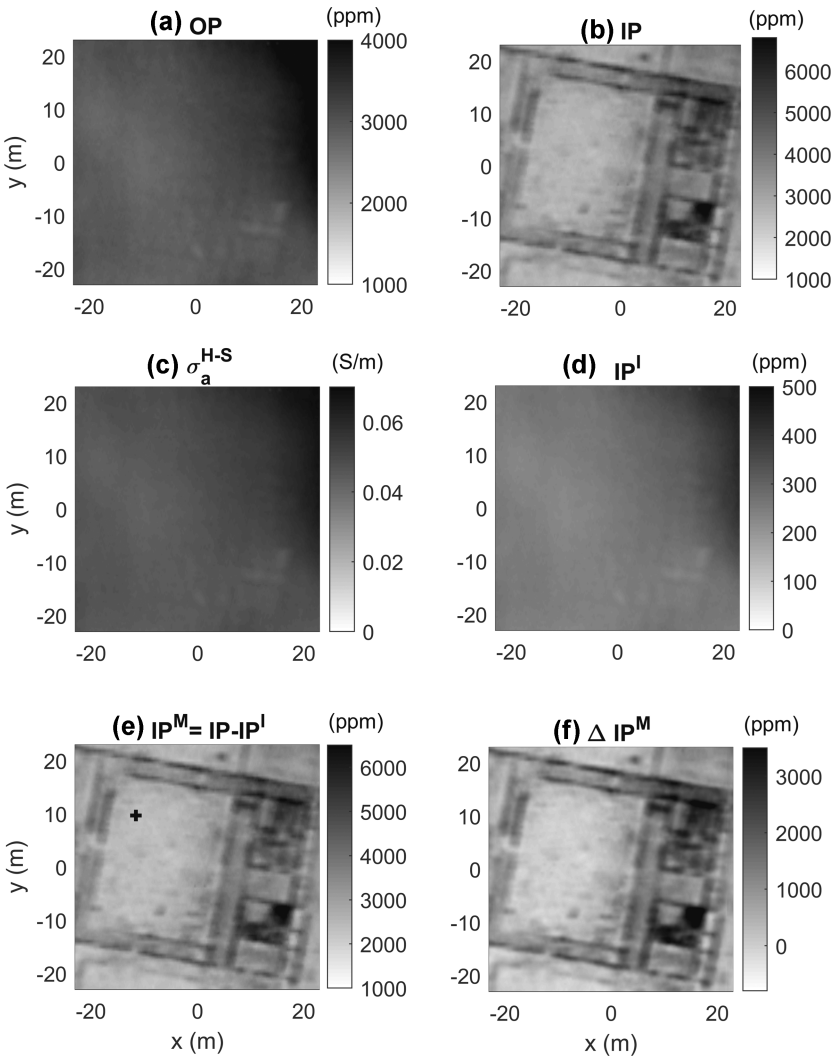

Figure 6. Details of the pre-processing steps for the HCP2 channel. (a) and (b) are the recorded OP and IP responses, respectively. Panel (c) is the half-space apparent conductivity σ_a^{H-S} computed with the OP response using the full (non-approximated) theory (Guillemoteau *et al.* 2016). (d) is the predicted induction fraction of the in-phase response, which was computed from the half-space apparent conductivity map. (e) is the remaining IP^M response after subtraction of the induction fraction. (f) is the anomalous IP^M field obtained with the reference point shown as a black cross in graphic (e).

HCP1 and HCP2 channels, which show no anomalies, we can retain the second option. Indeed, because the HCP1 and HCP2 have positive sensitivities near the surface, they should also show a positive anomaly in case of option 1. This example illustrates how such a four-configuration data set can remove some interpretation ambiguities regarding depth and how it forms an adequate data set to be inverted in the aim of getting a more quantitative information about the distribution of the magnetic susceptibility in the subsurface.

4.5 Results of the 3-D MCD imaging procedure

We apply the 3-D MCD approach to our field data set by using the same inversion settings as used for the synthetic experiments. The model grid is laterally extended (from $x, y = -24$ m to $x, y = 24$ m) in order to consider the entire area covered by data. After the inversion, we compute a modeled data set with the resulting 3-D voxel-based magnetic susceptibility model and compare it to the observed data set (Fig. 7). In Fig. 8, we visualize the resulting magnetic susceptibility model by three selected horizontal slices, which describe the principal characteristics of the reconstructed subsurface. The shallowest slice (at a depth of $z = 0.1$ m) shows relatively low susceptibility materials and corresponds to the overburden soil layer. The second slice ($z = 0.4$ m) provides a high resolution image of the buried foundations. This result is in agreement with the fact that blocks of basalt are regularly outcropped by the farming activity, meaning that the top of basaltic walls is located at the basis of the ploughed layer over the whole field, that is, at nearly 30 cm depth. The deepest slice shows a more blurred image as expected from the theoretical loss of resolution with depth with such surface-based geophysical measurements. However, it unveils additional features that are different from the above slice in the most complex part of the field, that is, where the building is. Furthermore, it clearly highlights a less permeable body in the centre of the courtyard, which is not visible in the shallower parts of the model. This structure is related to the low susceptibility anomalies visible in the PERP1.1 and PERP2.1 data maps, which we have discussed above. This target can actually be validated by the aerial photography shown in Fig. 5d and corresponds to a former pool, which could have served for embellishing the internal yard, according to the archaeological data on this type of villa. In fact, we can observe a good correlation between

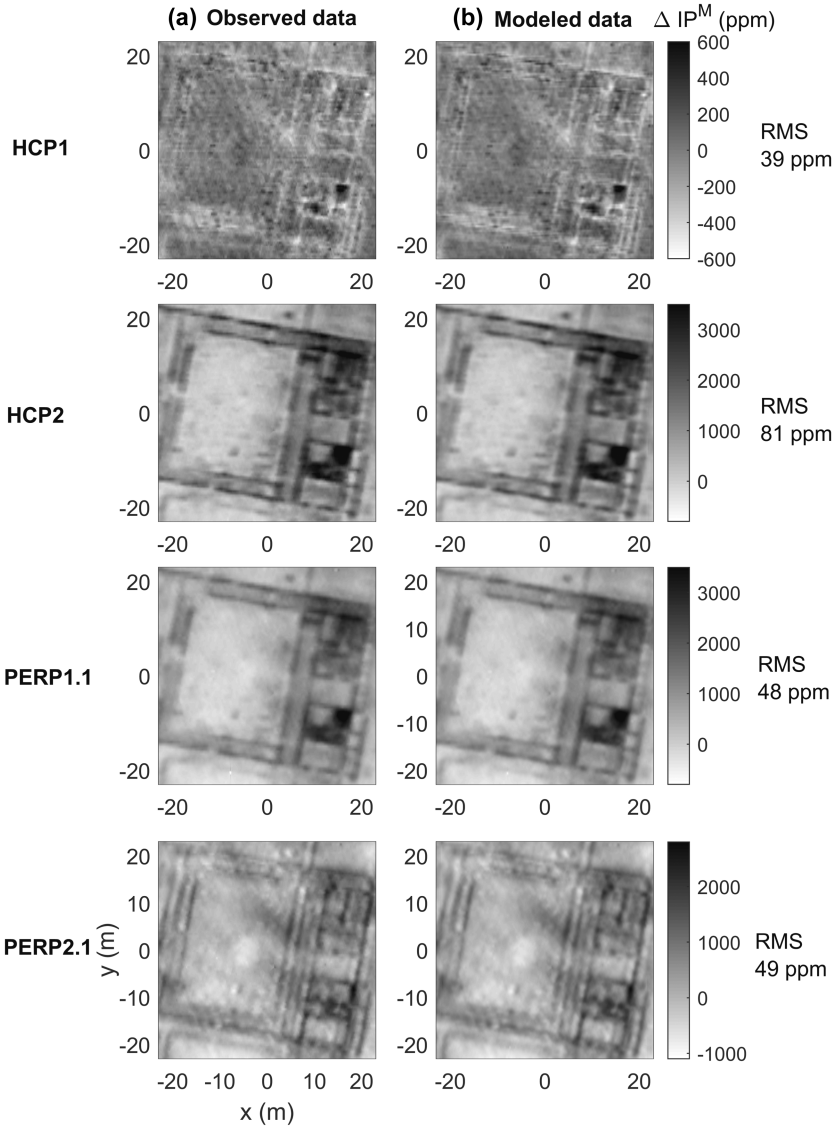

Figure 7. Field experiment at Lieu Dieu's archaeological site : comparison between (a) the observed data and (b) the modeled data computed after the 3-D MCD inversion. We show the RMS error for each channel on the right side. The global RMS error including the four channels is 57 ppm.

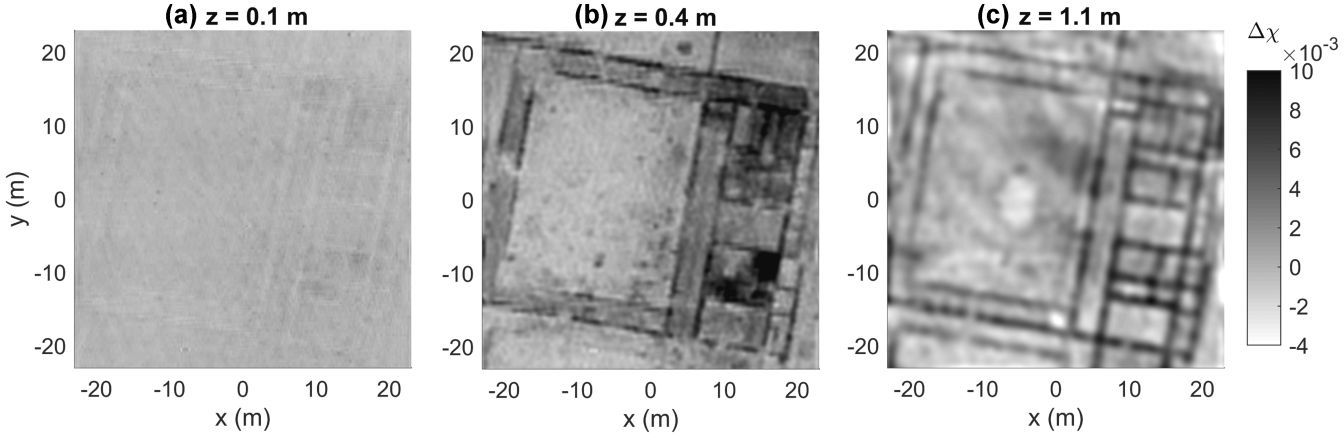

Figure 8. Result of the 3-D MCD imaging procedure for a fraction of the Gallo-Roman villa of Lieu Dieu, Auvergne (France). Here, we show three horizontal slices of the resulting 3-D voxel-based model of magnetic susceptibility. a) Shallow slice at $z = 0.1$ m resulting from the less permeable upper soil layer. (b) Intermediate slice at $z = 0.4$ m characterizing the top part of the foundations. (c) Deeper slice at $z = 1.1$ m characterizing the lower part of the foundations as well as a deep less permeable structure located at the centre of the courtyard.

the susceptibility anomaly and the colour of the vegetation at the surface. The yellow crop mark corresponds to a water stress caused by the basaltic foundations and is obviously correlated with positive susceptibility contrasts in the geophysical model. Inversely, the dark green crop mark is typically associated to a higher content of water and/or organic matter in the subsurface, which is likely to be caused by the pool's remains. As expected from the susceptibility of such materials, it is well correlated to negative susceptibily contrasts in the geophysical model. Thanks to our 3-D imaging procedure, we have now a better idea of its relative depth with regard to the villa foundations for eventual future excavation work.

Our results show that most of the basic features of the villa were retrieved by the 3-D MCD imaging, which could provide rather detailed depth and lateral information about its different components across a relatively large area. This makes our method a practical tool for both an exploration context (as typically expected from archaeogeophysical survey) and a more focused study, which could be done to help the excavation phase.

5 DISCUSSION

We show here a case of application of an active source magnetic method by considering the in-phase data collected by a loop–loop frequency domain EMI rigid sensor to study rather highly magnetic targets, at shallow depths.

In a context of exploration of less magnetic targets, this method could be more limited than the well established (passive) magnetic method as it may not detect low susceptibility contrasts. However, for the detected anomalies, the active magnetic method offers the possibility to characterize the depth of the sources. Furthermore, it can help in estimating the type (induced or remnant) of magnetization for targets that are visible with both the passive and the active magnetic methods. We can therefore say that the active magnetic method gives useful information complementary to the passive magnetic method.

Larger depths can theoretically be reached by using loop–loop systems working with decametric coil spacings. These systems work with a non rigid setup and by this fact, contain more noise related to the positioning and the orientation of the coils. However, by applying new acquisition practices including more precise positioning of the transmitter and the receiver(s), one may be able to image more extended and deeper susceptibility contrast with such systems.

The MCD approach presented in this study assumes a constant inversion kernel over the whole surveyed areas. This implies acquisition at a constant height and a flat ground surface at the scale of the lateral footprint of the soundings. For the system used in this study, we can fairly say that wavelengths of topography superior to 5 m do not affect the robustness of the MCD approach. This means that in such a context, we can assume a flat ground surface for the whole surveyed area and simply drape the results according to the topography. In presence of microtopography with metre or submetre wavelengths, one solution is to reduce its effect on the recorded data by increasing the height of the system. By this way, the measurements will be less sensitive to the shallow contrasts related to the topography. If this is not possible, one needs to reduce the topography effect before applying the MCD approach. If the microtopography is caused by linear tracks resulting from farming activities as ploughing, it can be easily removed by applying a directional filter to the data maps. For the case of a more complex pattern of microtopography, one may need to forward model the related effect on the data given a prior knowledge of the conductivity and the susceptibility of the affected layer, and to subtract it from the data before inversion. This approach is then similar to typical topographic corrections as found in potential field methods. Another choice is to use a standard spatial domain inversion, which can directly formulate the model space according to the topography. However, as already mentionned in the introduction, inverting typical data sets by setting a spatial domain model space that is fine enough to properly model the microtopography is also difficult to put in operation due to the expected large time and memory costs.

6 CONCLUSION

We present a framework for the 3-D imaging of the subsurface magnetic permeability/susceptibility, which is based on the inversion of in-phase data sets collected by portable loop–loop electromagnetic sensors. In order to avoid any aliasing effect in the procedure of interpretation, we obviously suggest to fulfill the basic sampling theorem when collecting the data. This means to record data sets with a higher lateral sampling than typically done in practice with such systems.

For the pre-processing of the data, the induction fraction and the temporal drifts of the in-phase response need first to be removed in order to get only the magnetization fraction; the latter being interpretable with a linear magneto-static theory. To avoid any problems of channel miss-calibration, we suggest to invert an anomalous magnetic in-phase field with respect to a reference point collected in a homogeneous and non-susceptible area. We then apply a voxel-grid based 3-D multichannel deconvolution procedure, which permits the instantaneous inversion of large data sets, composed of more than a hundred thousand data points.

We performed several synthetic experiments and one real field application involving a four-configuration EMI system. The synthetic tests have shown that our imaging algorithm is robust and versatile, for a large range of subsurface distributions. This is necessary in an exploratory context, where no detailed prior information is available over the whole surveyed areas. Our procedure finds direct applications on detailed imaging of the subsurface in permeable bedrock environments as in volcanic areas.

The real field case study is an example of such applications. Indeed, the presented procedure allowed us to estimate the depths and shapes of basaltic walls buried in the first 2 m of the subsurface with submetre resolution capabilities. Besides its usefulness in a context of archaeological prospecting, our method opens the door to more focused and detailed characterization of the subsurface, which could also be used to design further excavation work.

Finally, we can say that our procedure of acquisition and inversion of EMI sensor data allows the characterization of the subsurface magnetic permeability/susceptibility at high spatial resolution and computation efficiency. Thanks to the on-going and expected future progresses in term of in-phase signal/noise ratio collected by EMI instruments, our method also appears to be a promising approach to image environments with low susceptibility contrasts, as found in non-volcanic areas.

ACKNOWLEDGEMENTS

We thank Niklas Allroggen and Florian Dorgerloh for helping us in collecting the data. We also thank INRAP for partly supporting our field operations in Auvergne through the project 'ArchEM', and the *Direction Regionale des Affaires Culturelles (DRAC) Auvergne*

Rhône-Alpes for administrating and authorizing our field experiment at the archaeological site of Lieu Dieu. Finally, we are grateful to the owner of the field that holds the Gallo-Roman villa who kindly let us accessing his land.

REFERENCES

Baasch, B., Müller, H., Oberle, F. & Dobeneck, T.V., 2014. Inversion of marine multifrequency electromagnetic profiling data: a new approach to resolve surficial sediment stratification, *Geophys. J. Int.,* **200**(1), 439–451.

Benech, C. & Marmet, E., 1999. Optimum depth of investigation and conductivity response rejection of the different electromagnetic devices measuring apparent magnetic susceptibility, *Archaeol. Prospect.,* **6**(1), 31–45.

Benech, C., Tabbagh, A. & Desvignes, G., 2002. Joint inversion of EM and magnetic data for near-surface studies, *Geophysics,* **67**(6), 1729–1739.

Böniger, U. & Tronicke, J., 2010. On the potential of kinematic GPR surveying using a self-tracking total station: evaluating system crosstalk and latency, *IEEE Trans. Geosci. Rem. Sens.,* **48,** 3792–3798.

Constable, S.C., Parker, R.L. & Constable, C.G., 1987. Occams inversion: a practical algorithm for generating smooth models from electromagnetic sounding data, *Geophysics,* **52,** 289–300.

de Hoop, A.T., 1995. *Handbook of Radiation and Scattering of Waves,* Academic Press.

Delefortrie, S., De Smedt, P., Saey, T., Van de Vijver, E. & Van Meirvenne, M., 2014. An efficient calibration procedure for correction of drift in EMI survey data, *J. appl. Geophys.,* **110,** 115–125.

Delefortrie, S., Hanssens, D. & De Smedt, P., 2018. Low signal-to-noise FDEM in-phase data: practical potential for magnetic susceptibility modelling, *J. appl. Geophys.,* **152,** 17–25.

Farquharson, C.G., Oldenburg, D.W. & Routh, P.S., 2003. Simultaneous 1D inversion of loop-loop electromagnetic data for magnetic susceptibility and electrical conductivity, *Geophysics,* **68,** 1857–1869.

Guillemoteau, J. & Tronicke, J., 2015. Non-standard ground conductivity meter configurations: evaluating sensitivities and applicability, *J. appl. Geophys.,* **118,** 15–23.

Guillemoteau, J. & Tronicke, J., 2016. Evaluation of a rapid hybrid spectral-spatial domain 3D forward modelling approach for loop-loop electromagnetic induction quadrature data acquired in low-induction-number environments, *Geophysics,* **81**(6), E447–E458.

Guillemoteau, J., Sailhac, P., Boulanger, C. & Trules, J., 2015. Inversion of ground constant offset loop-loop electromagnetic data for a large range of induction numbers, *Geophysics,* **80,** E11–E21.

Guillemoteau, J., Simon, F.X., Lück, E. & Tronicke, J., 2016. 1D sequential inversion of portable multi-configuration electromagnetic induction data, *Near Surf. Geophys.,* **14,** 411–420.

Guillemoteau, J., Christensen, N.B., Jacobsen, B.H. & Tronicke, J., 2017. Fast 3D multichannel deconvolution of electromagnetic induction loop-loop apparent conductivity data sets acquired at low induction numbers, *Geophysics,* **82**(6), E357–E369.

Huang, H. & Won, I.J., 2000. Conductivity and susceptibility mapping using broadband electromagnetic sensors, *J. Environ. Eng. Geophys.,* **5,** 31–41.

Huang, J., Minasny, B., Whelan, B.M., McBratney, A.B. & Triantafilis, J., 2017. Temperature-dependent hysteresis effects on EM induction instruments: an example of single-frequency multi-coil array instruments, *Comput. Electr. Agric.,* **132,** 76–85.

Kamm, J., Becken, M. & Pedersen, L.B., 2013. Inversion of slingram electromagnetic induction data using a Born approximation, *Geophysics,* **78,** 208–212.

Klose, T., Guillemoteau, J., Simon, F.-X. & Tronicke, J., 2018. Toward subsurface magnetic permeability imaging with electromagnetic induction sensors: sensitivity computation and reconstruction of measured data, *Geophysics,* **83**(5), 1–46.

Li, Y. & Oldenburg, D.W., 1992. Approximate inverse mappings in DC resistivity problems, *Geophys. J. Int.,* **109**(2), 343–362.

McNeill, J.D., 1980. Electromagnetic terrain conductivity measurements at low induction numbers, Technical Note TN-6, Geonics Ltd.

Møller, I., Jacobsen, B.H. & Christensen, N.B., 2001. Rapid inversion of 2-D geoelectrical data by multichannel deconvolution, *Geophysics,* **66,** 800–808.

Noh, K., Chung, Y., Seol, S.J., Byun, J. & Uchida, T., 2014. Three-dimensional inversion of CSEM data: water leak detection using a small-loop EM method, *J. appl. Geophys.,* **102,** 134–144.

Noh, K., Oh, S., Seol, S.J., Lee, K.H. & Byun, J., 2016. Analysis of anomalous electrical conductivity and magnetic permeability effects using a frequency domain controlled-source electromagnetic method, *Geophys. J. Int.,* **204**(3), 1550–1564.

Noh, K., Lee, K.H., Oh, S., Seol, S.J. & Byun, J., 2017. Numerical evaluation of active source magnetics as a method for imaging high-resolution near-surface magnetic heterogeneity, *Geophysics,* **82**(5), J27–J38.

Noh, K., Oh, S., Seol, S.J. & Byun, J., 2018. 3D sequential inversion of frequency-domain airborne electromagnetic data to determine conductive and magnetic heterogeneities, *Geophysics,* **83**(5), E357–E369.

Pérez-Flores, M.A., Antonio-Carpio, R.G., Gómez-Trevino, E., Ferguson, I. & Méndez-Delgado, S., 2012. Imaging of 3D electromagnetic data at low-induction numbers, *Geophysics,* **77,** WB47–WB57.

Sasaki, Y., Kim, J. & Cho, S., 2010. Mulitdimensional inversion of loop-loop frequency-domain EM data for resistivity and magnetic susceptibility, *Geophysics,* **75,** 213–223.

Simon, F.X., Dousteyssier, B., Pareilh-Peyrou, M., Labazuy, P., Donnadieu, F., Guillemoteau, J., Alfredo Mayoral, P. & Vautier, F., 2016. Nouvelles données archéologiques sur l'occupation du sol durant l'Antiquité de la Narse de la Sauvetat (63) , *Journée Régionale de l'Archéologie (Auvergne)*, June 2016, Clermont-Ferrand, France. https://hal-clermont-univ.archives-ouvertes.fr/hal-02069183.

Simpson, D., Van Meirvienne, M., lück, E., Rühlmann, J., Say, T. & Bourgeois, J., 2010. Sensitivity of multi-coil frequency domain electromagnetic induction sensors to map soil magnetic susceptibility, *Eur. J. Soil Sci.,* **61,** 469–478.

Tabbagh, A., 1985. The response of three dimensional magnetic and conductive body in shallow depth E.M. prospecting, *Geophys. J. R. astr. Soc.,* **81,** 215–230.

Tabbagh, A., 1986. Applications and advantages of the Slingram electromagnetic method for archaeological prospecting, *Geophysics,* **51,** 576–584.

Thiesson, J., Kessouri, P., Schamper, C. & Tabbagh, A., 2014. Calibration of frequency-domain electromagnetic devices used in near-surface surveying, *Near Surf. Geophys.,* **12,** 481–491.

Thiesson, J., Tabbagh, A., Simon, F.-X. & Dabas, M., 2017. 3d linear inversion of magnetic susceptibility data acquired by frequency domain emi, *J. appl. Geophys.,* **136,** 165–177.

Tite, M. & Mullins, C., 1970. Electromagnetic prospecting on archaeological sites using a soil conductivity meter, *Archaeometry,* **12**(1), 97–104.

Vallat, P., 2002. Histoire de l'occupation du sol dans la Limagne des buttes (Puy-de-Dôme) de l'âge du Fer à l'Antiquité tardive, *PhD thesis*, Université d'Avignon et des Pays du Vaucluse.